NANO LETTERS

pubs.acs.org/NanoLett Letter

Unveiling Efficient Acousto-Optic Modulation in Silicon Photonic Devices via Lithium Niobate Using Transfer Printing

Siyu Xu, Weixin Liu, Xianhao Le, and Chengkuo Lee*

Cite This: *Nano Lett.* 2024, 24, 12964−12972 Read Online

ACCESS | Metrics & More | Article Recommendations | Supporting Information

ABSTRACT: Piezo-optomechanics presents a promising route to convert microwave signals to the optical domain, implementing processing tasks that are challenging using conventional electronics. The surge of integrated photonics facilitates the exploitation of localized light−sound interactions toward new technological paradigms. However, efficient acousto-optic interaction has yet to be fully exploited in silicon due to the absence of piezoelectricity, despite its maturity in photonic integrated circuits. Here, we introduce a distinctive acousto-optic scheme to supplement silicon photonic devices through heterogeneous integration with lithium niobate (LN). Utilizing LN as an efficient acoustic pump to harness the inherently exceptional photoelasticity in silicon, we demonstrate efficient microwave-to-acoustic transduction, ultimately achieving a modulation figure-of-merit of $V_{\pi}L \sim 0.496$ V·cm. This efficient modulation scheme is further extended to implement non-reciprocal intermodal modulation. The proposed hybrid integration route opens new possibilities for tailoring photon−phonon interactions in silicon, consolidating acousto-optic technology in multifunctional integrated photonics.

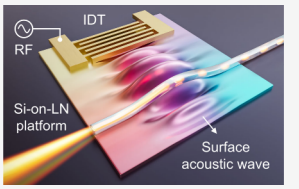

KEYWORDS: *acousto-optic modulator, piezo-optomechanics, silicon photonics, lithium niobate, transfer printing, mid-infrared*

The generation, transmission, and manipulation of high-speed radiofrequency (RF) signals using optical means, widely known as microwave photonics (MWP), have become an area of utmost interest recently.[1] MWP has unlocked a new paradigm for signal processing with unprecedented bandwidth afforded by the frequency upconversion of microwaves to the optical domain.[2] In particular, piezo-optomechanics provides an efficient interface between light and microwave-driven acoustic waves on piezoelectric media, facilitating signal conversion among different degrees of freedom.[3−5]

Building on decades of legacy in discrete components, the rejuvenation of the acousto-optic technology is paralleled by the surge of integrated photonics, in which localized optical and mechanical modes can be strongly coupled within wavelength-scale.[6−8] Recent advances in photonic integrated circuits (PICs) have propelled acousto-optic technologies to new heights with landmark demonstrations ranging from traditional uses in microwave tunable filters,[9,10] frequency shifters,[11] and modulators,[12] to emerging fields such as gyroscope,[13] beam deflection in light detection and ranging (LiDAR) systems,[14] frequency-domain optical computing,[15] and quantum information science.[16] Emerging technologies on non-reciprocity due to photon−phonon interactions promise new capabilities of MWP systems to achieve directional routing and blocking, or to mitigate multipath interference in communication.[17−19] Advances in the bandwidth, loss, and isolation metrics of the proof-of-principle investigation reveal the highly competitive potential of acousto-optic technology for practical optical isolators, provided that microwave-to-acoustic conversion efficiency can reach a satisfactory level.[20−22]

The implementation of efficient microwave-to-optical transduction, preferably in silicon—the predominant material in PICs—is deemed indispensable for information processing and manipulation in an ultracompact footprint, especially given silicon's inherently prominent photoelastic coefficient. However, acousto-optic devices have been considerably less exploited in silicon due to the absence of piezoelectricity. The past decade has witnessed significant efforts to enable the excitation of acoustic waves in silicon, relying on strategies such as stimulated Brillouin scattering[23] and laser-triggered thermoelastic expansion.[24] The relatively inefficient scattering in these devices limits their practical utility. Particularly, on the single-material (monolithic) platform, realizing the most efficient electrically driven acousto-optic modulation necessitates the simultaneously optimized piezoelectric and optomechanical coupling, which is limited strictly to the inherent material properties. The exploration of chip-level integration using multi-material (heterogeneous or hybrid) opens a new avenue through strategic combinations of materials, specifically leveraging one for enhanced piezoelectric coupling and another for optimized optomechanical coupling.[25] To fundamentally unveil the compelling photoelasticity in silicon, inducing powerful acoustic pumps via external piezoelectric materials is deemed effective and

Received: July 27, 2024
Revised: September 16, 2024
Accepted: September 16, 2024
Published: September 20, 2024

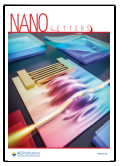

https://doi.org/10.1021/acs.nanolett.4c03622
Nano Lett. 2024, 24, 12964−12972

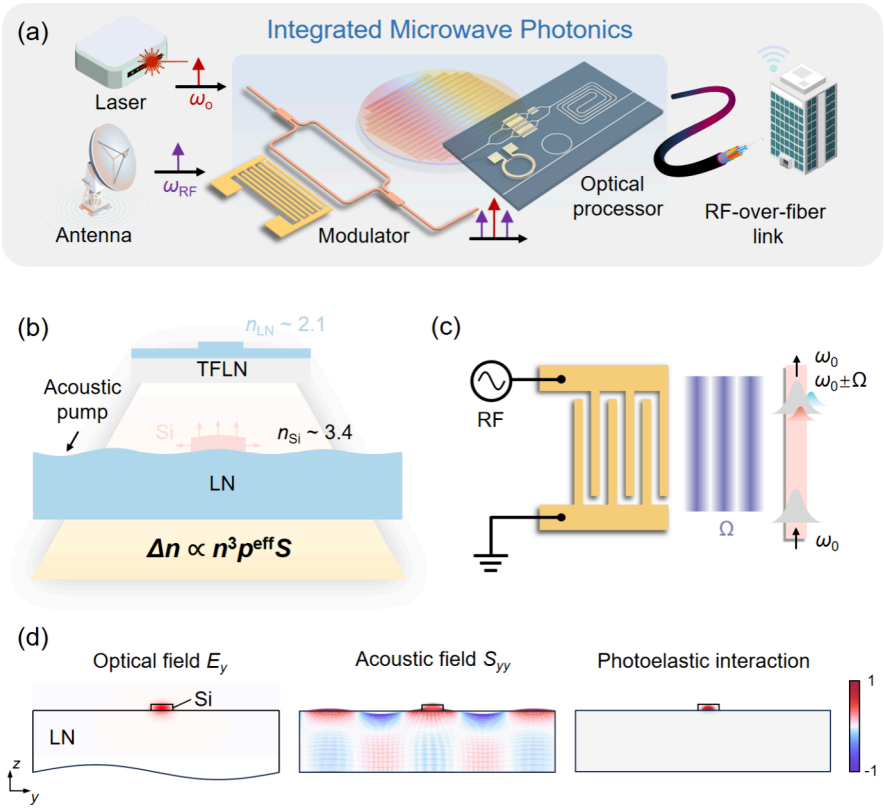

Figure 1. Application and principle of integrated acousto-optic modulator built on silicon photonic devices. (a) A radiofrequency (RF) wireless network scenario relying on an integrated microwave photonics system. RF signals acquired from an antenna can be converted coherently to the optical domain through an on-chip acousto-optic modulator, thereby upconverting the spectrum to optical frequencies. The optical signal can then be seamlessly processed using an integrated optical signal processor, ultimately transported over an RF-over-fiber link. (b) The proposed heterogeneously integrated acousto-optic configuration, leveraging the LN substrate as an acoustic pump for enhanced piezoelectric coupling and the overlaid silicon waveguide with a larger refractive index for optimized optomechanical coupling. TFLN, thin-film lithium niobate. p^{eff}, effective photoelastic coefficient. (c) The basic principle of the acousto-optic phase modulation. An on-chip interdigital transducer (IDT) is driven by an external RF source at frequency Ω, inducing optical energy transfer to frequency-detuned optical sidebands at $\omega_0 \pm \Omega$. (d) Numerical finite-element simulation of the acoustic-optic interaction: dominant electric field E_y of the fundamental quasi-transverse-electric (TE) mode (left), dominant S_{yy} component of the acoustic strain field (middle), and the resulting photoelastic interaction representing optical refractive index change (right), visualized by multiplying E_y and S_{yy}. Color scale bars are normalized individually.

preferable.[26−29] Given its remarkable piezoelectric and photoelastic properties as well as minimal mechanical and optical losses, lithium niobate (LN) has been considered as an ideal active material for both the generation and propagation of acoustic waves in planar PICs.[30−33] Combining mature silicon photonics with prominent piezoelectric LN transducers thus emerges as an attractive approach.[34]

In this work, we heterogeneously combine silicon and LN via a reliable, flexible transfer printing technique to construct integrated acousto-optic devices, fully leveraging the intrinsically prominent photoelasticity of silicon and the superior piezoelectricity of LN. While high-quality LN wafers are used as a representative demonstration for unparalleled acoustic excitation, this transfer printing scheme is nonmaterial-selective, enabling micro- and nanomaterials with distinctive functions to be assembled on various platforms in a massively parallel manner, including well-established thin-film-lithium-niobate (TFLN) technology. The hybrid acousto-optic configuration provides a more robust and compatible fabrication method that eliminates the necessity for etching foreign piezoelectric materials and suspended structures,[35,36] allowing effortless access to numerous "silicon-on-anything" platforms. We extend the operating wavelength to the mid-infrared (MIR) spectral range around 4 μm, a regime that significantly lags behind in the development of integrated acousto-optic components, despite rich applications in spectroscopy, selective sensing, and free-space communication.[37−40] The modulation metric of $V_\pi L \sim 0.496$ V·cm outperforms most existing on-chip electro-optic technologies and is already comparable to state-of-the-art acousto-optic modulators at near-infrared wavelengths, especially considering that this metric scales with the operating wavelength.[41] We thereafter exploit the effective interaction to form electrically driven non-reciprocal devices via intermodal transition, with isolation contrast up to 12 dB observed. We envisage that all these demonstrated features in the Si/LN hybrid platform will collectively supplement the standard silicon photonic devices, with the prospect of bridging future RF wireless networks and the canonical integrated MWP systems (Figure 1a).

DESIGN CONCEPT

Despite LN featuring a relatively considerable photoelastic coefficient ($p_{31} = 0.179$), the overall magnitude of the acoustically induced refractive index Δn, proportional to n^3 (see Supplementary Note 1), is diminished by its low refractive index ($n \sim 2.1$). In contrast, silicon ($n \sim 3.4$, $p_{11} = -0.094$), serving as an excellent waveguide-guiding layer, enables

https://doi.org/10.1021/acs.nanolett.4c03622
Nano Lett. 2024, 24, 12964−12972

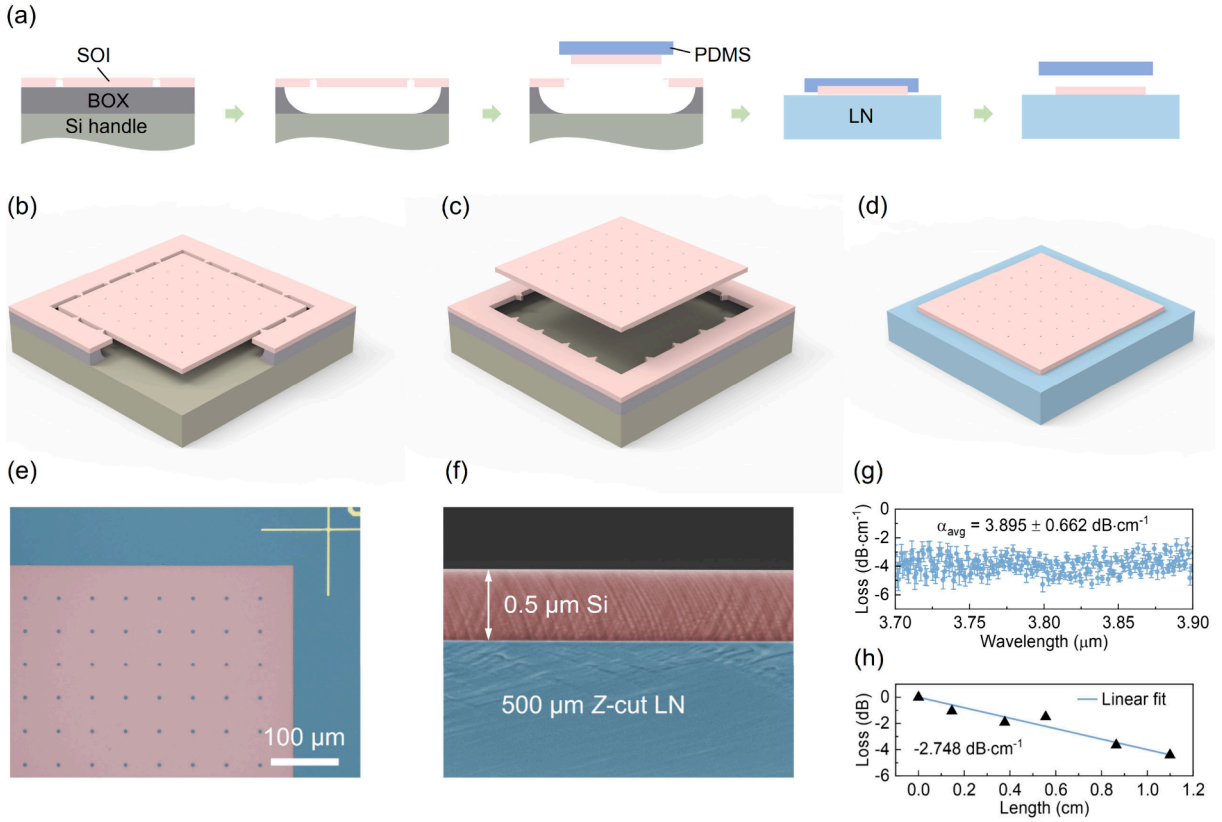

Figure 2. Heterogenous integration of a Si-on-LN platform based on transfer printing. (a) Generic form of transfer printing, relying on kinetically controlled adhesion of an elastomeric PDMS stamp. (b) Prefabrication of the structured silicon components with tethers for connection and arrays of holes for facilitating wet etching of the sacrificial oxide layer underneath. (c) Retrieval of the free-standing silicon thin film using an elastomeric stamp by breaking the tethers. (d) Delivery of the silicon layer onto the target LN substrate through direct adhesive bonding. (e) False-colored microscope image of the as-fabricated Si-on-LN platform. (f) False-colored scanning electron microscope image of its cross-section (blue: LN; pink: Si). (g) Propagation loss of Si-on-LN hybrid waveguides. (h) Representative linear fitting of cut-back measurement results at 3.874 μm.

enhanced light−sound interactions through integration with LN substrates (Figure 1b). The basic operation scheme for linear acousto-optic modulation through traveling-wave optomechanical coupling is depicted in Figure 1c, which can be straightforwardly conceptualized as strain-induced phase shift of the incident optical carrier with zero acoustic momentum along the waveguide axis. A high-quality Z-cut LN crystal was selected to harness high electromechanical coupling, as well as for its isotropic in-plane refractive indices, which allow for unrestricted layouts of optical waveguides upon bending. The Rayleigh surface acoustic wave (SAW) mode on piezoelectric media is a low-loss elastic wave capable of inducing a perturbation to the refractive index, typically through a combination of the moving boundary effect and the primary photoelastic effect (also known as the elasto-optic effect) ubiquitous in all dielectric media, along with the secondary electro-optic effect in noncentrosymmetric materials (see Supplementary Note 2). Finite element analysis based on the device geometry and the crystal orientation is indicated in Figure 1d. The quasi-transverse-electric (TE) mode was employed to confine the optical field predominantly in silicon (left), simultaneously benefiting large photoelasticity and tightly confined optical fields. Notably, the strain is effectively transferred to the silicon waveguide (middle), while the acoustic traveling wave remains well preserved after the interaction, owing to the high-velocity contrast between silicon and LN. The coupling strength of the acousto-optic interaction is quantitatively evaluated through spatial overlap factor Γ, by integrating the products of the optical field $E(y, z)$ and acoustic strain components S_j against their respective coupling coefficients (p_{ij} tensors) following:

$$\Gamma \propto \frac{\iint \sum p_{ij} S_j |E(y, z)|^2 \mathrm{d}y\mathrm{d}z}{\iint |E(y, z)|^2 \mathrm{d}y\mathrm{d}z} \quad (1)$$

The distribution of the dominant photoelastic perturbation is depicted in the right column of Figure. 1d.

DEVICE FABRICATION

Transfer printing has attracted considerable interest as one of the representative heterogeneous integration techniques for integrated photonics, facilitating the deterministic assembly of lasers, amplifiers, modulators, and detectors into a single device.[42−46] Based on this idea, we developed a simple yet robust integration route, specifically transferring silicon onto LN, ultimately forming a hybrid photonic platform. In general, the process involves the preparation, retrieval (pick-up), and delivery (printing) steps, illustrated in Figure 2a (for details see Methods). The process started with a standard silicon-on-insulator (SOI) wafer, with buried oxide (BOX) and device layer thickness of 2 and 0.5 μm, respectively. During the prefabrication, the structured components including tethers (for connections) and an array of holes (for facilitating wet etching) were defined on the source chip (Figure 2b). The underlying SiO_2 layer served as a sacrificial layer, which can be

https://doi.org/10.1021/acs.nanolett.4c03622
Nano Lett. 2024, 24, 12964−12972

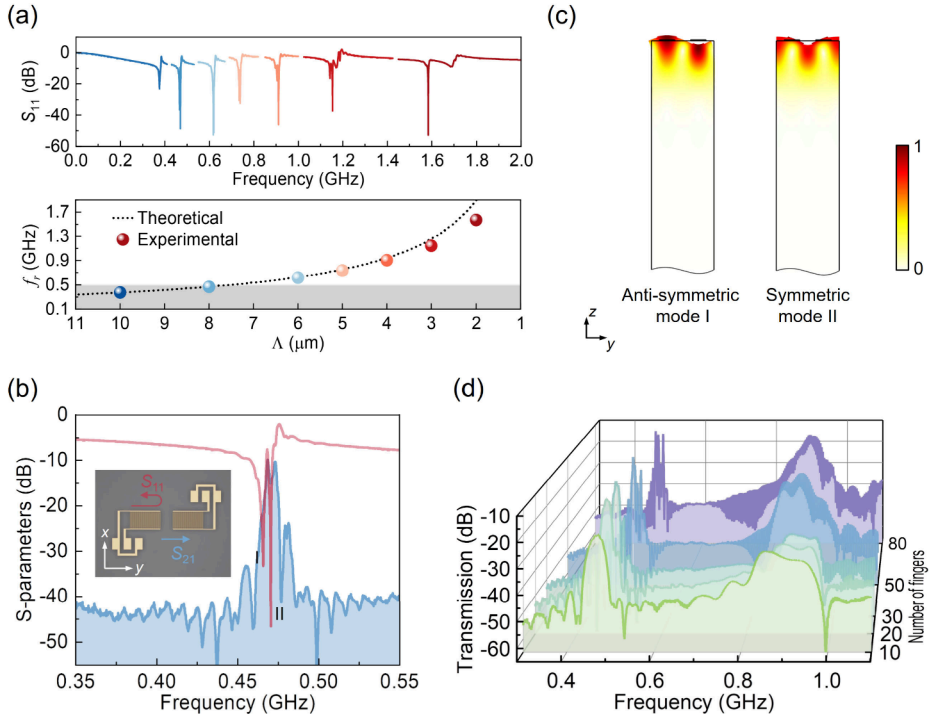

Figure 3. Characterization of microwave-to-acoustic transduction. (a) The top subpanel shows the measured electrical reflection S_{11} spectra of the IDTs. The corresponding resonance frequencies f_r of the fundamental modes for each transducer are summarized in the lower panel. The gray-shaded area denotes the bandwidth of the photodetector employed in the subsequent experiment, above which the acousto-optic response will decrease significantly. (b) Measured reflection S_{11} and transmission S_{21} spectra of an IDT pair with 8 μm pitch. A minimum reflection of −46.66 dB indicates a near-unity conversion efficiency. Inset: optical microscope image of the surface acoustic wave (SAW) transmitter and receiver. (c) Displacement profiles at two eigen-frequencies, referred to as symmetric and antisymmetric SAW modes depending on the symmetry of the out-of-plane displacement with respect to the centerline. (d) Transmission spectra of IDTs with different numbers of electrode finger pairs.

selectively etched with dilute hydrofluoric (HF) acid, thereby making the silicon layer free-standing.[47] The structure was then subjected to critical point drying to prevent liquid-to-vapor transitions that could otherwise lead to collapse (Supplementary Note 3). Next, an elastomeric polydimethylsiloxane (PDMS) stamp was used to retract the monocrystalline silicon from the source chip by breaking tethers in a controlled manner (Figure 2c). This silicon layer was subsequently printed onto the receiver LN through direct adhesive bonding, primarily governed by the van der Waals force (Figure 2d). The as-fabricated silicon-on-lithium-niobate (Si-on-LN) platform allows for standard processes such as lithography, etching, and metallization. The false-colored microscope image in Figure 2e shows the printed silicon thin film (in pink) on the LN substrate (in blue), showcasing its uniform surface, with the cross-section depicted in Figure 2f. As a measure of fundamental optical performance, propagation loss was characterized using the conventional cut-back method with waveguides of varying lengths. An average propagation loss of 3.895 ± 0.662 dB·cm^{-1} across the depicted wavelengths was observed (Figure 2g), primarily attributed to scattering related to the waveguide sidewall roughness and potentially improvable, with the representative linear fitting of data demonstrating an optimal 2.748 dB·cm^{-1} (Figure 2h).

MICROWAVE-TO-ACOUSTIC TRANSDUCTION

The acoustic pump is excited through an interdigital transducer (IDT) fabricated on piezoelectric LN substrates, enabling transduction between alternative electric fields and acoustic waves. To characterize the microwave-to-acoustic transduction, the spatial periods of the IDT electrodes, defined as transducer pitch Λ, were fabricated in the range of 2−12 μm without loss of generality. The electrical reflection spectra S_{11} of these transducers, near their fundamental Rayleigh modes, were individually measured using a vector network analyzer (VNA) and presented in the upper panel of Figure 3a. Extremely narrowband dips indicate efficient transduction of acoustic waves when the frequencies of the probing microwave match those of propagating SAWs. The frequencies corresponding to the fundamental modes for each transducer are recorded in the lower panel. The SAW frequency reaches 1.584 GHz for Λ = 2 μm while maintaining a minimum reflection of −52.76 dB. The excitation approach is generic and can be, in principle, extended to higher frequencies by further scaling transducer pitches. In practice, the characterizations for acousto-optic interaction at MIR wavelength were limited by the bandwidth of the commercially available photodetector (VIGO Photonics PVI-4TE-4, 3 dB-bandwidth ∼0.45 GHz), making direct observation of preserved modulation performance unattainable. Therefore, a pitch of 8 μm was used for the subsequent acousto-optic modulation characterization, resulting in a peak coupling efficiency of the fundamental mode occurring around 0.46 GHz. The y-propagating SAW was selected for the optimal combination of electromechanical coupling efficiency and acoustic loss (see Supplementary Note 4).

A representative characterization for a SAW delay line, consisting of a pair of identical 8 μm-pitch IDTs separated by a distance of 20 pitches, is shown in Figure 3b. The results indicate that the highest transmission of S_{21} = −9.879 dB was

https://doi.org/10.1021/acs.nanolett.4c03622
Nano Lett. 2024, 24, 12964−12972

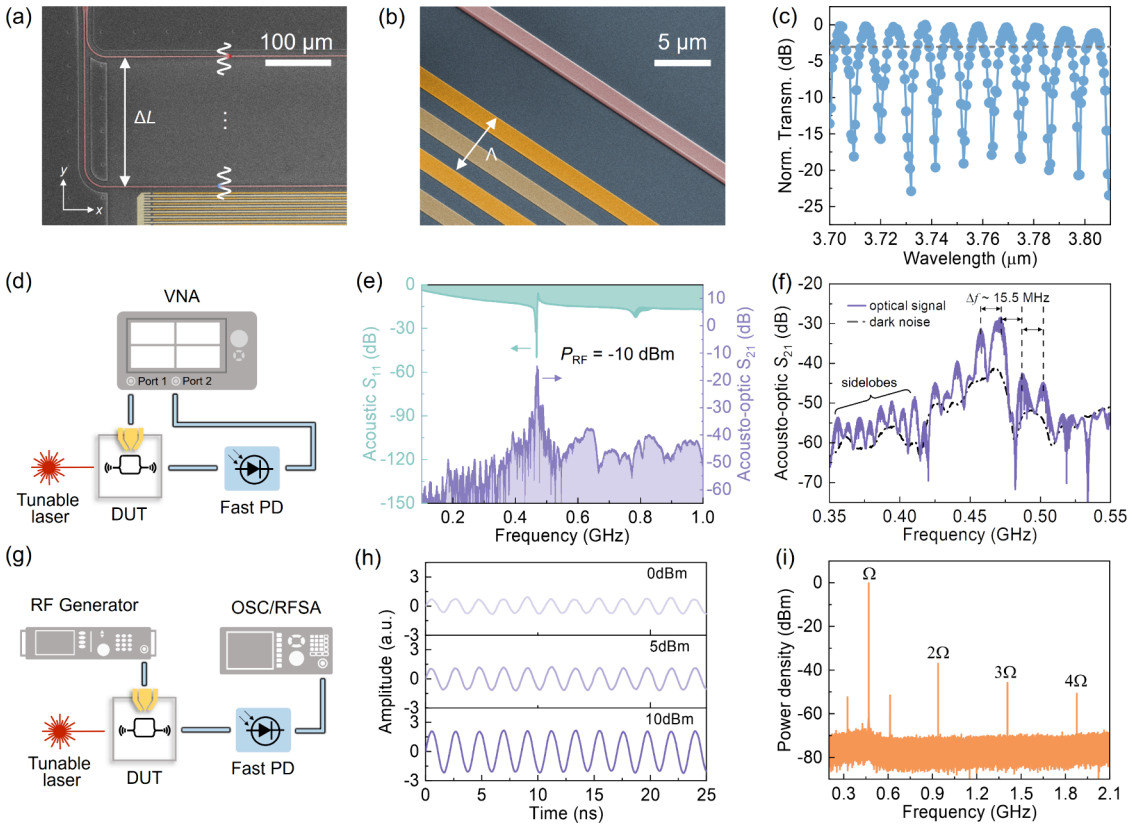

Figure 4. Characterization of the acousto-optic modulation. (a) False-colored scanning electron microscope image of an acousto-optic Mach−Zehnder interferometer (MZI) which is unbalanced to allow optical phase control. (b) A magnified, tilted view of the central part of the MZI with the IDT adjacent to the waveguide. (c) Optical transmission of the acousto-optic MZI. (d) Simplified experimental schematic for obtaining frequency response. DUT, device under test; VNA, vector network analyzer; PD, photodetector. (e) Experimental acoustic S_{11} and acousto-optic S_{21} spectra. (f) A characteristic fringing pattern measured from the transducer with a broader bandwidth (composed of 30 pairs of fingers). The dashed line illustrates the background noise level, measured when the laser is inactive. (g) Simplified experimental schematic for measuring temporal microwave-to-photonic response. OSC, oscilloscope; RFSA, RF spectrum analyzer. (h) Optical response under modulation with varying microwave power. (i) Power density spectrum of the optical readout with an applied microwave power of 20 dBm. The spurious sidebands spaced from the first harmonic of ∼144 MHz may be attributed to noise from the setup.

obtained. Here, the transmission loss is primarily attributed to an intrinsic −6 dB reflection in the symmetric IDT design due to bidirectional SAW actuation (3 dB for each IDT), along with load-dependent reflectivity and electrode resistivity. A minimum reflection of −46.66 dB corresponds to the optimal microwave-to-acoustic conversion efficiency (otherwise termed mismatch efficiency,[36] calculated as 1 - S_{11}) greater than 99.99%. Remarkably, two nearly coincident acoustic modes are observed, consistent with the eigenmodes calculated from the simulations (symmetric mode I and antisymmetric mode II in Figure 3c). The electromechanical coupling coefficient k^2, which represents the fraction of the mechanical power in the acoustic mode transduced from the input microwave power,[6] is obtained as 4.82% for the fundamental Rayleigh mode (see the derivation in Supplementary Note 5). This value is comparable to the k^2 coefficients observed in other crystal orientations.[48] Considering strong reflection comes at the expense of reduced microwave-to-acoustic transduction bandwidth, we designed 50 pairs of IDT fingers sufficiently large to ensure efficient energy conversion, thereby yielding a high-quality-factor acoustic resonance (Figure 3d).

■ ACOUSTO-OPTIC MODULATION

We experimentally characterized the proposed acousto-optic configuration using a typical unbalanced Mach−Zehnder interferometer (MZI) with an optical path difference of $2\Delta L$, which translates the acousto-optic phase modulation to an amplitude response (Figure 4a). A magnified, tilted view of the MZI arm with an adjacent IDT is shown in Figure 4b, where elastic waves with frequency Ω are incident perpendicularly with respect to the optical propagation axis. The waveguide width w is 1.8 μm in these devices and the nominal aperture of IDT is 1 mm. Without reflection boundaries in the unpatterned LN layer, traveling acoustic waves can interact with optical waves in both arms with minimal acoustic loss, effectively inducing strain in a distributed manner. As the induced index changes cancel out when both arms experience the same tensile/compressive strain, ΔL is set as an odd multiple of the acoustic wavelength Λ (as illustrated schematically in blue/red in Figure 4a). To evaluate the acousto-optic modulation characteristics, the probing wavelength of the laser was chosen to correspond to a $\pi/2$ phase difference between the two optical paths (as indicated by the dashed line in Figure 4c). The schematic of experimental setups is shown in Figure 4d, where the driving port (port 1) of the VNA was connected to the IDT and the receiving port (port 2) was connected to the photodetector. In the acquired acousto-optic S_{21} spectrum, peaks corresponding to acoustic modes are observed at frequencies that align well with sharp dips in the acoustic S_{11}

https://doi.org/10.1021/acs.nanolett.4c03622
Nano Lett. 2024, 24, 12964−12972

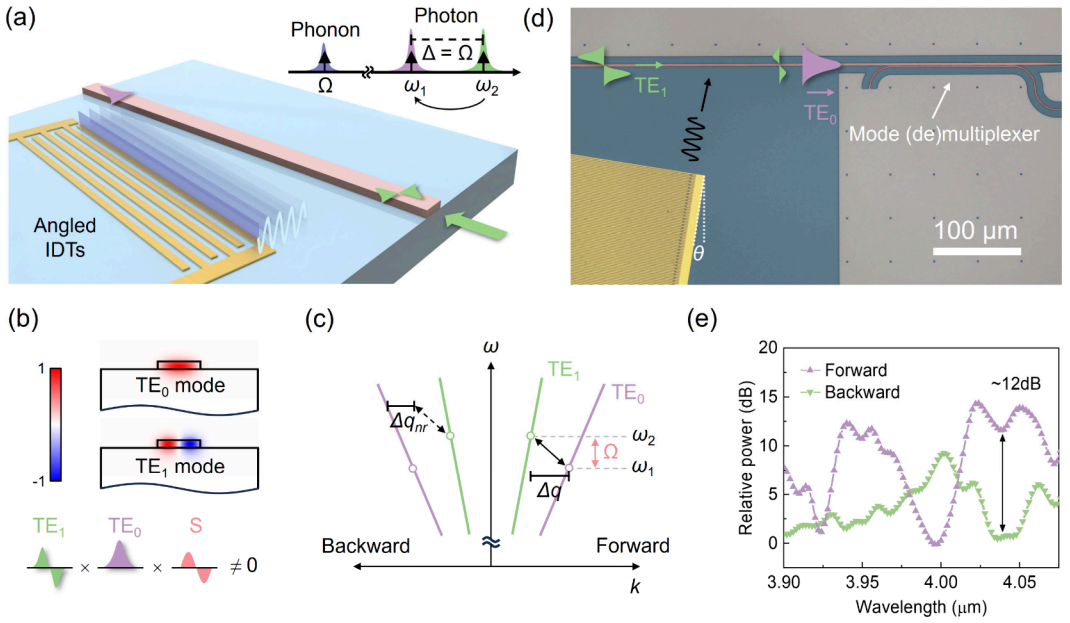

Figure 5. Non-reciprocal intermodal modulation. (a) Device operation concept. An angled acoustic wave simultaneously breaks orthogonality between the optical modes for effective intermodal conversion and produces a nonzero axial phonon momentum for phase-matching. The inset shows a frequency-domain representation of the indirect intermodal transition. (b) Illustration of the transverse mode profiles of TE_0 and TE_1, indicating an odd acoustic pump profile is essential to obtain the nonzero overlap integral. (c) ω-k diagram describing the origin of non-reciprocity. For forward propagation, intermodal scattering is phase-matched around frequency ω_2, while in the backward direction, a wavevector mismatch Δq_{nr} inhibits modulation at the same frequency. (d) Microscope image of an intermodal modulator with integrated mode (de)multiplexers composed of adiabatic tapers and asymmetric directional couplers. The acoustic wave was excited at an angle θ with respect to the normal optical axis. (e) Relative power ratio of mode conversion in forward and backward propagation, demonstrating non-reciprocal modulation.

spectrum at $\Omega/2\pi \sim 0.46$ GHz. One can further extrapolate the half-wave voltage V_π theoretically from S_{21} following:[7,36]

$$S_{21} = \left(\frac{\pi R_{PD} P_{out,0}^{opt}}{V_\pi}\right)^2 \tag{2}$$

in which R_{PD} is the responsivity of the photodetector and $P_{out,0}^{opt}$ is the direct current (DC) component of the optical readout at the selected wavelength. With a peak acousto-optic modulation amplitude of −14.85 dB occurring at 0.469 GHz (Figure 4e), the voltage-length metric $V_\pi L$ can be then calculated as 0.496 V·cm (for derivation see Supplementary Note 6). Notably, the performance of our acousto-optic device is fundamentally not limited by frequency and is expected to improve, provided that the operating frequency is not restricted by the deployed photodetector. More generally, the local phase modulation contributes to the overall output modulation efficiency depending on whether the acoustically induced optical phase delay between the two modulated segments contributes constructively or destructively. It leads to a characteristic frequency-domain interference pattern in the passband, which can be utilized to enhance acousto-optic modulation at specific frequencies. To better visualize the fringing pattern in the passband, an IDT with a broader bandwidth was placed adjacent to the same device. The acoustic velocity can be determined through the frequency difference Δf between the peaks of the passband ripples in Figure 4f, yielding a group velocity $v = \Delta L \times \Delta f = 3782$ m/s. To assess signal conversion fidelity, the microwave signal generated using the RF generator was fed into the IDT, and the optical readout was recorded using the oscilloscope and RF spectrum analyzer, respectively (Figure 4g). The distortion-free time-resolved dynamic responses in Figure 4h demonstrate the feasibility of the microwave-photonic conversion/modulation link for RF signal manipulation. By further increasing the microwave power to compensate for the degraded photodetection responsivity above gigahertz frequencies, the emergence of up to fourth-order modulation harmonics can be observed through the spectrum analyzer (Figure 4i). This result is consistent with the expected phase modulation nature of the acousto-optic interaction (see Supplementary Note 6).

NON-RECIPROCAL INTERMODAL MODULATION

In contrast to intramodal phase modulation, non-reciprocal modulation in acoustic means relies on intermediate mode conversion as an auxiliary degree of freedom for phase-matching (Figure 5a).[49] Given that optical frequencies are much higher than acoustic frequencies, the time-varying refractive-index perturbation induced by sound can be considered as a simple inhomogeneous medium. An electrically driven elastic wave, with frequency Ω incident at an angle θ with respect to the optical path, produces a nonzero axial wavevector q along the waveguide axis that satisfies momentum conservation (or equivalently, phase-matching condition). The intermodal optomechanical coupling coefficient is proportional to the spatial integral of the optical mode within the cross-section, which can be essentially described by the coupled mode theory as[22]

$$\kappa \propto \iint E_1(r_\perp) E_2(r_\perp) (\nabla \cdot u(r_\perp)) \mathrm{d}^2 r_\perp \tag{3}$$

where $E_1(r_\perp)$ and $E_2(r_\perp)$ are the cross-sectional electric fields of the TE_0 and TE_1 modes, respectively, and u is the displacement associated with acoustic strain. As illustrated in Figure 5b, the electric fields of the TE_0 and TE_1 modes exhibit odd (symmetric) and even (antisymmetric) shapes in the

https://doi.org/10.1021/acs.nanolett.4c03622
Nano Lett. 2024, 24, 12964−12972

transverse direction, respectively. The underlying concept of non-reciprocal scattering can be intuitively understood through the ω-k diagram in Figure 5c, which depicts the indirect intermodal transitions for both the forward- and backward-propagating optical signals. The transition is only supported in one direction due to the distinct dispersion of the TE_0 and TE_1 mode families, resulting in a non-reciprocal wavevector mismatch Δq_{nr}. The representative architecture for realizing intermodal modulation is shown in Figure 5d, in which (de)multiplexers are incorporated. We designed the bus waveguide as 3.4 μm wide to accommodate both TE_0 and TE_1 modes. To ensure nonzero overlap among a pair of copropagating modes, the acoustic displacement distribution must be asymmetric with respect to the center of the waveguide. To achieve an optimal intermodal interaction, the transverse acoustic wavelength Λ_t was hence set equal to the waveguide width w. The IDT pitch Λ is determined by $\Lambda_t\cos(\theta)$ with $\tan(\theta) = (\Lambda_t/2\pi)q$. We hereby fabricated IDTs oriented with $\theta = 9.325°$ and $\Lambda = 3.68$ μm (for further details see Supplementary Note 7 and ref 20). To experimentally characterize the non-reciprocal behavior of the devices, the RF driving frequency was fixed at $\Omega/2\pi = 1.038$ GHz with a power of 22.60 dBm, while injecting the probe light in either the forward or backward direction of a single device. An isolation ratio exceeding 12 dB in the relative power ratio of mode conversion (with and without SAW excitation) has been achieved (Figure 5e). Further gains in the isolation ratio are of importance and well within reach. By adopting a compact multisegment serpentine structure, longer interaction lengths leading to larger non-reciprocal mismatch $\Delta q_{nr}L$ allow further improvement.[20]

In conclusion, this work presents a reliable approach to exploiting the underutilized acousto-optic properties in silicon, specifically by integrating a silicon photonic layer with a piezoelectric LN layer using transfer printing. Optomechanical interactions that were once purely limited to intrinsic properties of monolithic platforms can now be accomplished from external piezoelectric materials with their own merits, targeting optimal performance. Owing to the substantial piezoelectricity in LN and the inherently outstanding photoelasticity in silicon, we have demonstrated a highly efficient acousto-optic modulator featuring a $V_\pi L$ of ∼0.496 V·cm. The outlined integration approach can be readily extended to any alternative substrates, allowing for more intriguing modes.[50−55] We further demonstrated that the strong photon−phonon coupling in silicon waveguides could be utilized to develop non-reciprocal modulation, which is envisioned to realize the full potential for expanding applications beyond telecom-related technologies. A promising example could involve waveguide-based broadband superluminescent diodes,[56] where the essential antireflection facet required to prevent optical feedback could be achieved using an integrated, electrically driven isolator. Such driving schemes, combined with the ease of integrating multiple components like sensors and photodetectors, could unlock exciting opportunities, including miniaturized MIR spectrometers and lab-on-a-chip technologies.[57−60]

METHODS

Device Fabrication. The acousto-optic devices were fabricated on standard (100)-oriented SOI wafers with a 500 nm-thick silicon device layer. During prefabrication, the structured components were defined with electron-beam lithography (EBL; JEOL JBX-6300FS 100 kV) using a high-resolution positive resist (ZEON ZEP-520A), and the pattern was subsequently transferred to silicon using deep reactive ion etching (DRIE, Oxford Plasmalab System 100). The residual polymer was decomposed by deep-ultraviolet irradiation (Digital UV Ozone System, Novascan PSD Pro Series) and removed by acetone. After the underneath BOX layer was wet-etched through HF, the prepared silicon thin film was transfer-printed onto a diced 10 mm × 10 mm Z-cut optical-grade LN crystal substrates with a thickness of 500 μm. Next, the Si-on-LN device underwent another step of spin-coating with ZEP-520A as well as a water-soluble conductive polymer ESPACER 300Z to mitigate the charging issue. After the second EBL exposure, the conductive polymer was removed by immersion in deionized water for 20 s, and the exposed resist was subsequently developed in amyl acetate for 90 s, followed by full etching of silicon using DRIE. The IDTs were patterned using the aforementioned exposure and development process flow, followed by the deposition of a 3 nm-thick/80 nm-thick titanium/gold stack using an electron-beam evaporator (AJA ATC-ORION-8E) and a lift-off process with acetone.

Optical Characterization. The input light was generated by a tunable quantum cascaded laser (Daylight Solutions, MIRcat-1200) covering the wavelength range from 3.65 to 4.15 μm. The optical polarization was adjusted to be TE polarized using a half-wave plate (Thorlabs, WPLQ05M-4000), and then coupled into a single-mode ZrF_4 optical fiber through a ZnSe lens. Two symmetric fiber holders were mounted on the input and output 6-axis stages at a 10° angle from vertical for alignment. The output light was directed into an HgCdTe (MCT) photovoltaic detector (Vigo System, PVI-4TE-4). During static characterization of optical transmission, an optical chopping system (Edmund Optics) placed at the laser output port, in combination with the lock-in amplifier (Stanford Research System, SR830), was employed to enhance the signal-to-noise ratio.

Mechanical Transduction and Characterization. The transduction efficiency of the IDTs was characterized using the standard approach with a vector network analyzer (Rohde & Schwarz ZNB20), which was calibrated using a set of impedance calibration standards (MPI calibration substrate AC2−2) to remove any effect of cables and RF probes (MPI T26A).

ASSOCIATED CONTENT

Supporting Information

The Supporting Information is available free of charge at https://pubs.acs.org/doi/10.1021/acs.nanolett.4c03622.

Analysis of photoelastic perturbation, electromechanical coupling and acousto-optic modulation efficiency, investigation of crystal orientation-dependent performance, phase-matching conditions for intermodal modulation, characterization of mode multiplexers, and performance comparison (PDF)

AUTHOR INFORMATION

Corresponding Author

Chengkuo Lee − *Department of Electrical & Computer Engineering, National University of Singapore, Singapore 117583, Singapore; Center for Intelligent Sensors and MEMS, National University of Singapore, Singapore 117608, Singapore; NUS Suzhou Research Institute (NUSRI),*

https://doi.org/10.1021/acs.nanolett.4c03622
Nano Lett. 2024, 24, 12964−12972

Suzhou, Jiangsu 215123, China; orcid.org/0000-0002-8886-3649; Email: elelc@nus.edu.sg

Authors

Siyu Xu − *Department of Electrical & Computer Engineering, National University of Singapore, Singapore 117583, Singapore; Center for Intelligent Sensors and MEMS, National University of Singapore, Singapore 117608, Singapore;* orcid.org/0009-0006-3777-9654

Weixin Liu − *Department of Electrical & Computer Engineering, National University of Singapore, Singapore 117583, Singapore; Center for Intelligent Sensors and MEMS, National University of Singapore, Singapore 117608, Singapore;* orcid.org/0000-0002-5526-3487

Xianhao Le − *Department of Electrical & Computer Engineering, National University of Singapore, Singapore 117583, Singapore; Center for Intelligent Sensors and MEMS, National University of Singapore, Singapore 117608, Singapore*

Complete contact information is available at: https://pubs.acs.org/10.1021/acs.nanolett.4c03622

Notes

The authors declare no competing financial interest.

■ ACKNOWLEDGMENTS

The authors would like to thank Bowei Dong for insightful discussions. This research was supported by the Singapore Ministry of Education Academic Research Fund Tier 2 (MOE-T2EP50220-0014), the RIE2025 MTC Industry Alignment Fund − Pre-Positioning Programme (M23M5a0069), and the National Research Foundation Competitive Research Programme (NRF-CRP28-2022-0002). The authors acknowledge the funding support from the National Semiconductor Translation and Innovation Centre (M24W1NS005) and the National Centre for Advanced Integrated Photonics (NRF-MSG-2023-0002) in Singapore.

■ REFERENCES

(1) Marpaung, D.; Yao, J.; Capmany, J. Integrated Microwave Photonics. *Nat. Photonics* **2019**, *13* (2), 80−90.
(2) Feng, H.; Ge, T.; Guo, X.; Wang, B.; Zhang, Y.; Chen, Z.; Zhu, S.; Zhang, K.; Sun, W.; Huang, C.; Yuan, Y.; Wang, C. Integrated Lithium Niobate Microwave Photonic Processing Engine. *Nature* **2024**, *627* (8002), 80−87.
(3) Zhu, D.; Shao, L.; Yu, M.; Cheng, R.; Desiatov, B.; Xin, C. J.; Hu, Y.; Holzgrafe, J.; Ghosh, S.; Shams-Ansari, A.; Puma, E.; Sinclair, N.; Reimer, C.; Zhang, M.; Lončar, M. Integrated Photonics on Thin-Film Lithium Niobate. *Adv. Opt. Photonics* **2021**, *13* (2), 242.
(4) Liu, X.; Bruch, A. W.; Tang, H. X. Aluminum Nitride Photonic Integrated Circuits: From Piezo-Optomechanics to Nonlinear Optics. *Adv. Opt. Photonics* **2023**, *15* (1), 236.
(5) Tian, H.; Liu, J.; Attanasio, A.; Siddharth, A.; Blesin, T.; Wang, R. N.; Voloshin, A.; Lihachev, G.; Riemensberger, J.; Kenning, S. E.; Tian, Y.; Chang, T. H.; Bancora, A.; Snigirev, V.; Shadymov, V.; Kippenberg, T. J.; Bhave, S. Piezoelectric Actuation for Integrated. *arXiv Photonics* **2024**, arXiv:2405.08836.
(6) Tadesse, S. A.; Li, M. Sub-Optical Wavelength Acoustic Wave Modulation of Integrated Photonic Resonators at Microwave Frequencies. *Nat. Commun.* **2014**, *5* (1), 5402.
(7) Shao, L.; Yu, M.; Maity, S.; Sinclair, N.; Zheng, L.; Chia, C.; Shams-Ansari, A.; Wang, C.; Zhang, M.; Lai, K.; Lončar, M. Microwave-to-Optical Conversion Using Lithium Niobate Thin-Film Acoustic Resonators. *Optica* **2019**, *6* (12), 1498.
(8) Chen, I.-T.; Li, B.; Lee, S.; Chakravarthi, S.; Fu, K.-M.; Li, M. Optomechanical Ring Resonator for Efficient Microwave-Optical Frequency Conversion. *Nat. Commun.* **2023**, *14* (1), 7594.
(9) Katzman, M.; Munk, D.; Priel, M.; Grunwald, E.; Hen, M.; Inbar, N.; Feldberg, M.; Sharabani, T.; Zektzer, R.; Bashan, G.; Vofsi, M.; Levy, U.; Zadok, A. Surface Acoustic Microwave Photonic Filters in Standard Silicon-on-Insulator. *Optica* **2021**, *8* (5), 697.
(10) Kim, H.; Shin, H. Active Information Manipulation via Optically Driven Acoustic-Wave Interference. *Nano Lett.* **2021**, *21* (17), 7270−7276.
(11) Shao, L.; Sinclair, N.; Leatham, J.; Hu, Y.; Yu, M.; Turpin, T.; Crowe, D.; Lončar, M. Integrated Microwave Acousto-Optic Frequency Shifter on Thin-Film Lithium Niobate. *Opt. Express* **2020**, *28* (16), 23728.
(12) Poveda, A. C.; Bühler, D. D.; Sáez, A. C.; Santos, P. V.; de Lima, M. M. Semiconductor Optical Waveguide Devices Modulated by Surface Acoustic Waves. *J. Phys. D. Appl. Phys.* **2019**, *52*, No. 253001.
(13) Mahmoud, M.; Mahmoud, A.; Cai, L.; Khan, M.; Mukherjee, T.; Bain, J.; Piazza, G. Novel on Chip Rotation Detection Based on the Acousto-Optic Effect in Surface Acoustic Wave Gyroscopes. *Opt. Express* **2018**, *26* (19), 25060.
(14) Li, B.; Lin, Q.; Li, M. Frequency−Angular Resolving LiDAR Using Chip-Scale Acousto-Optic Beam Steering. *Nature* **2023**, *620* (7973), 316−322.
(15) Zhao, H.; Li, B.; Li, H.; Li, M. Enabling Scalable Optical Computing in Synthetic Frequency Dimension Using Integrated Cavity Acousto-Optics. *Nat. Commun.* **2022**, *13* (1), 5426.
(16) Han, X.; Fu, W.; Zhong, C.; Zou, C.-L.; Xu, Y.; Sayem, A. Al; Xu, M.; Wang, S.; Cheng, R.; Jiang, L.; Tang, H. X. Cavity Piezo-Mechanics for Superconducting-Nanophotonic Quantum Interface. *Nat. Commun.* **2020**, *11* (1), 3237.
(17) Lawrence, M.; Dionne, J. A. Nanoscale Nonreciprocity via Photon-Spin-Polarized Stimulated Raman Scattering. *Nat. Commun.* **2019**, *10* (1), 3297.
(18) Hu, T.; Shao, H.; Yang, L.; Xu, C.; Yang, M.; Yu, H.; Jiang, X.; Yang, J. Four-Port Silicon Multi-Wavelength Optical Router for Photonic Networks-on-Chip. *IEEE Photonics Technol. Lett.* **2013**, *25* (23), 2281−2284.
(19) Fang, K.; Luo, J.; Metelmann, A.; Matheny, M. H.; Marquardt, F.; Clerk, A. A.; Painter, O. Generalized Non-Reciprocity in an Optomechanical Circuit via Synthetic Magnetism and Reservoir Engineering. *Nat. Phys.* **2017**, *13* (5), 465−471.
(20) Kittlaus, E. A.; Jones, W. M.; Rakich, P. T.; Otterstrom, N. T.; Muller, R. E.; Rais-Zadeh, M. Electrically Driven Acousto-Optics and Broadband Non-Reciprocity in Silicon Photonics. *Nat. Photonics* **2021**, *15* (1), 43−52.
(21) Tian, H.; Liu, J.; Siddharth, A.; Wang, R. N.; Blésin, T.; He, J.; Kippenberg, T. J.; Bhave, S. A. Magnetic-Free Silicon Nitride Integrated Optical Isolator. *Nat. Photonics* **2021**, *15* (11), 828−836.
(22) Sohn, D. B.; Kim, S.; Bahl, G. Time-Reversal Symmetry Breaking with Acoustic Pumping of Nanophotonic Circuits. *Nat. Photonics* **2018**, *12* (2), 91−97.
(23) Kittlaus, E. A.; Otterstrom, N. T.; Rakich, P. T. On-Chip Inter-Modal Brillouin Scattering. *Nat. Commun.* **2017**, *8* (1), No. 15819.
(24) Munk, D.; Katzman, M.; Hen, M.; Priel, M.; Feldberg, M.; Sharabani, T.; Levy, S.; Bergman, A.; Zadok, A. Surface Acoustic Wave Photonic Devices in Silicon on Insulator. *Nat. Commun.* **2019**, *10* (1), 4214.
(25) Wan, L.; Yang, Z.; Zhou, W.; Wen, M.; Feng, T.; Zeng, S.; Liu, D.; Li, H.; Pan, J.; Zhu, N.; Liu, W.; Li, Z. Highly Efficient Acousto-Optic Modulation Using Nonsuspended Thin-Film Lithium Niobate-Chalcogenide Hybrid Waveguides. *Light Sci. Appl.* **2022**, *11* (1), 145.
(26) Huang, C.; Shi, H.; Yu, L.; Wang, K.; Cheng, M.; Huang, Q.; Jiao, W.; Sun, J. Acousto-Optic Modulation in Silicon Waveguides Based on Piezoelectric Aluminum Scandium Nitride Film. *Adv. Opt. Mater.* **2022**, *10* (6), No. 2102334.
(27) Bian, K.; Li, Z.; Liu, Y.; Xu, S.; Zhao, X.; Qiu, Y.; Dong, Y.; Zhong, Q.; Wu, T.; Zheng, S.; Hu, T. Demonstration of Acousto-

Optical Modulation Based on a Thin-Film AlScN Photonic Platform. *Photonics Res.* **2024**, *12* (6), 1138.
(28) Ansari, I.; George, J. P.; Feutmba, G. F.; Van de Veire, T.; Pandey, A.; Beeckman, J.; Van Thourhout, D. Light Modulation in Silicon Photonics by PZT Actuated Acoustic Waves. *ACS Photonics* **2022**, *9* (6), 1944−1953.
(29) Marinković, I.; Drimmer, M.; Hensen, B.; Gröblacher, S. Hybrid Integration of Silicon Photonic Devices on Lithium Niobate for Optomechanical Wavelength Conversion. *Nano Lett.* **2021**, *21* (1), 529−535.
(30) Pan, B.; Liu, H.; Huang, Y.; Yu, Z.; Li, H.; Shi, Y.; Liu, L.; Dai, D. Perspective on Lithium-Niobate-on-Insulator Photonics Utilizing the Electro-Optic and Acousto-Optic Effects. *ACS Photonics* **2023**, *10* (7), 2078−2090.
(31) Yu, Z.; Sun, X. Acousto-Optic Modulation of Photonic Bound State in the Continuum. *Light Sci. Appl.* **2020**, *9* (1), 1.
(32) Khan, M. S. I.; Mahmoud, A.; Cai, L.; Mahmoud, M.; Mukherjee, T.; Bain, J. A.; Piazza, G. Extraction of Elastooptic Coefficient of Thin-Film Arsenic Trisulfide Using a Mach−Zehnder Acoustooptic Modulator on Lithium Niobate. *J. Light. Technol.* **2020**, *38* (7), 2053−2059.
(33) Shao, L.; Zhu, D.; Colangelo, M.; Lee, D.; Sinclair, N.; Hu, Y.; Rakich, P. T.; Lai, K.; Berggren, K. K.; Lončar, M. Electrical Control of Surface Acoustic Waves. *Nat. Electron.* **2022**, *5* (6), 348−355.
(34) Klopfer, E.; Dagli, S.; Barton, D.; Lawrence, M.; Dionne, J. A. High-Quality-Factor Silicon-on-Lithium Niobate Metasurfaces for Electro-Optically Reconfigurable Wavefront Shaping. *Nano Lett.* **2022**, *22* (4), 1703−1709.
(35) Cai, L.; Mahmoud, A.; Khan, M.; Mahmoud, M.; Mukherjee, T.; Bain, J.; Piazza, G. Acousto-Optical Modulation of Thin Film Lithium Niobate Waveguide Devices. *Photonics Res.* **2019**, *7* (9), 1003.
(36) Hassanien, A. E.; Link, S.; Yang, Y.; Chow, E.; Goddard, L. L.; Gong, S. Efficient and Wideband Acousto-Optic Modulation on Thin-Film Lithium Niobate for Microwave-to-Photonic Conversion. *Photonics Res.* **2021**, *9* (7), 1182.
(37) Hu, T.; Dong, B.; Luo, X.; Liow, T.-Y.; Song, J.; Lee, C.; Lo, G.-Q. Silicon Photonic Platforms for Mid-Infrared Applications [Invited]. *Photonics Res.* **2017**, *5* (5), 417.
(38) Kazakov, D.; Letsou, T. P.; Beiser, M.; Zhi, Y.; Opačak, N.; Piccardo, M.; Schwarz, B.; Capasso, F. Active Mid-Infrared Ring Resonators. *Nat. Commun.* **2024**, *15* (1), 607.
(39) Zhou, H.; Li, D.; Ren, Z.; Xu, C.; Wang, L.-F.; Lee, C. Surface Plasmons-Phonons for Mid-Infrared Hyperspectral Imaging. *Sci. Adv.* **2024**, *10* (22), No. eado3179.
(40) Dong, B.; Luo, X.; Zhu, S.; Hu, T.; Li, M.; Hasan, D.; Zhang, L.; Chua, S. J.; Wei, J.; Chang, Y.; Ma, Y.; Vachon, P.; Lo, G.-Q.; Ang, K. W.; Kwong, D.-L.; Lee, C. Thermal Annealing Study of the Mid-Infrared Aluminum Nitride on Insulator (AlNOI) Photonics Platform. *Opt. Express* **2019**, *27* (14), 19815.
(41) Zhang, M.; Wang, C.; Kharel, P.; Zhu, D.; Lončar, M. Integrated Lithium Niobate Electro-Optic Modulators: When Performance Meets Scalability. *Optica* **2021**, *8* (5), 652.
(42) Roelkens, G.; Zhang, J.; Bogaert, L.; Soltanian, E.; Billet, M.; Uzun, A.; Pan, B.; Liu, Y.; Delli, E.; Wang, D.; Oliva, V. B.; Ngoc Tran, L. T.; Guo, X.; Li, H.; Qin, S.; Akritidis, K.; Chen, Y.; Xue, Y.; Niels, M.; Maes, D.; Kiewiet, M.; Reep, T.; Vanackere, T.; Vandekerckhove, T.; Lufungula, I. L.; De Witte, J.; Reis, L.; Poelman, S.; Tan, Y.; Deng, H.; Bogaerts, W.; Morthier, G.; Van Thourhout, D.; Kuyken, B. Present and Future of Micro-Transfer Printing for Heterogeneous Photonic Integrated Circuits. *APL Photonics* **2024**, *9*, No. 010901, DOI: 10.1063/5.0181099.
(43) Ma, Y.; Chang, Y.; Dong, B.; Wei, J.; Liu, W.; Lee, C. Heterogeneously Integrated Graphene/Silicon/Halide Waveguide Photodetectors toward Chip-Scale Zero-Bias Long-Wave Infrared Spectroscopic Sensing. *ACS Nano* **2021**, *15* (6), 10084−10094.
(44) Chang, Y.; Xu, S.; Dong, B.; Wei, J.; Le, X.; Ma, Y.; Zhou, G.; Lee, C. Development of Triboelectric-Enabled Tunable Fabry-Pérot Photonic-Crystal-Slab Filter towards Wearable Mid-Infrared Computational Spectrometer. *Nano Energy* **2021**, *89*, No. 106446.
(45) Xu, S.; Ren, Z.; Dong, B.; Zhou, J.; Liu, W.; Lee, C. Mid-Infrared Silicon-on-Lithium-Niobate Electro-Optic Modulators Toward Integrated Spectroscopic Sensing Systems. *Adv. Opt. Mater.* **2023**, *11*, No. 2202228.
(46) Vanackere, T.; Vandekerckhove, T.; Bogaert, L.; Billet, M.; Poelman, S.; Cuyvers, S.; Van Kerrebrouck, J.; Moerman, A.; Caytan, O.; Singh, N.; Lemey, S.; Torfs, G.; Ossieur, P.; Roelkens, G.; Clemmen, S.; Kuyken, B. Heterogeneous Integration of a High-Speed Lithium Niobate Modulator on Silicon Nitride Using Micro-Transfer Printing. *APL Photonics* **2023**, *8*, No. 086102.
(47) Sun, H.; Qiao, Q.; Lee, C.; Zhou, G. MEMS-enabled Ultralow Power Consumption Programmable Arbitrary Order Mode Switch. *Laser Photon. Rev.* **2024**, DOI: 10.1002/lpor.202400641.
(48) Morgan, D.; Paige, E. G. S. *Surface Acoustic Wave Filters: With Applications to Electronic Communications and Signal Processing*; Elsevier, 2007. DOI: 10.1016/B978-0-12-372537-0.X5000-6.
(49) Sarabalis, C. J.; Van Laer, R.; Patel, R. N.; Dahmani, Y. D.; Jiang, W.; Mayor, F. M.; Safavi-Naeini, A. H. Acousto-Optic Modulation of a Wavelength-Scale Waveguide. *Optica* **2021**, *8* (4), 477.
(50) Sarabalis, C. J.; McKenna, T. P.; Patel, R. N.; Van Laer, R.; Safavi-Naeini, A. H. Acousto-Optic Modulation in Lithium Niobate on Sapphire. *APL Photonics* **2020**, *5* (8), No. 086104.
(51) Wang, C.; Li, Z.; Riemensberger, J.; Lihachev, G.; Churaev, M.; Kao, W.; Ji, X.; Zhang, J.; Blesin, T.; Davydova, A.; Chen, Y.; Huang, K.; Wang, X.; Ou, X.; Kippenberg, T. J. Lithium Tantalate Photonic Integrated Circuits for Volume Manufacturing. *Nature* **2024**, *629* (8013), 784−790.
(52) Shao, S.; Luo, Z.; Lu, Y.; Mazzalai, A.; Tosi, C.; Wu, T. High Quality Co-Sputtering AlScN Thin Films for Piezoelectric Lamb-Wave Resonators. *J. Microelectromechanical Syst.* **2022**, *31* (3), 328−337.
(53) Zhang, L.; Cui, C.; Chen, P.-K.; Fan, L. Integrated-Waveguide-Based Acousto-Optic Modulation with Complete Optical Conversion. *Optica* **2024**, *11* (2), 184.
(54) Du, M.; Huang, F.; Li, J.; Liu, Y.; Xu, X.; Wang, N.; Wu, T. Asymmetrical Lamb Wave Mode Resonant Infrared Detector Based on Lithium Niobate Thin Film. *Appl. Phys. Lett.* **2024**, *124*, No. 192202.
(55) Zhu, S.; Zhong, Q.; Li, N.; Hu, T.; Dong, Y.; Xu, Z.; Zhou, Y.; Fu, Y. H.; Singh, N. Integrated ScAlN Photonic Circuits on Silicon Substrate. In *Conference on Lasers and Electro-Optics*; Optica Publishing Group: Washington, D.C., 2020; p STu3P.5.
(56) Hou, C.-C.; Chen, H.-M.; Zhang, J.-C.; Zhuo, N.; Huang, Y.-Q.; Hogg, R. A.; Childs, D. T. D.; Ning, J.-Q.; Wang, Z.-G.; Liu, F.-Q.; Zhang, Z.-Y. Near-Infrared and Mid-Infrared Semiconductor Broadband Light Emitters. *Light Sci. Appl.* **2017**, *7* (3), 17170−17170.
(57) Zhang, Z.; Liu, X.; Zhou, H.; Xu, S.; Lee, C. Advances in Machine-Learning Enhanced Nanosensors: From Cloud Artificial Intelligence Toward Future Edge Computing at Chip Level. *Small Struct.* **2024**, *5* (4), No. 2300325.
(58) Liu, W.; Ma, Y.; Liu, X.; Zhou, J.; Xu, C.; Dong, B.; Lee, C. Larger-Than-Unity External Optical Field Confinement Enabled by Metamaterial-Assisted Comb Waveguide for Ultrasensitive Long-Wave Infrared Gas Spectroscopy. *Nano Lett.* **2022**, *22* (15), 6112−6120.
(59) Liu, X.; Zhang, Z.; Zhou, J.; Liu, W.; Zhou, G.; Lee, C. Artificial Intelligence-Enhanced Waveguide "Photonic Nose"- Augmented Sensing Platform for VOC Gases in Mid-Infrared. *Small* **2024**, *20* (24), No. 2400035.
(60) Zhou, J.; Liu, X.; Zhou, H.; Xu, S.; Xie, J.; Xu, C.; Liu, W.; Zhang, Z.; Lee, C. Artificial-Intelligence-Enhanced Mid-infrared Lab-on-a-Chip for Mixture Spectroscopy Analysis. *Laser Photon. Rev.* **2024**, DOI: 10.1002/lpor.202400754.

https://doi.org/10.1021/acs.nanolett.4c03622
Nano Lett. 2024, 24, 12964−12972